Experimental and numerical investigation of the interaction of the first four SH guided wave modes with symmetric and non-symmetric discontinuities in plates

Alan C. Kubrusly[a], Jean Pierre von der Weid[a] and Steve Dixon[b]

[a.] Centre for Telecommunication Studies, Pontifical Catholic University of Rio de Janeiro, Rio de Janeiro, 22451-900, Brazil; alan@cpti.cetuc.puc-rio.br
[b.] Department of Physics, University of Warwick, Coventry, CV4 7AL, UK; S.M.Dixon@warwick.ac.uk

***Abstract*—The interaction of the SH0, SH1, SH2 and SH3 guided wave modes on a metal plate with a thickness discontinuity is numerically and experimentally investigated. Two different geometries were evaluated, namely symmetric and non-symmetric discontinuities, relative to the plate longitudinal mid-plane. Experiments were performed with periodic permanent magnet array EMATs as transmitters and receivers. Mode separation in transmission and reception was experimentally and numerically performed by dual transduction and by modal decomposition post-processing techniques, respectively. The reflection and transmission coefficients at the discontinuity for each of the investigated SH modes was calculated. It has been experimentally confirmed that when interacting with symmetric discontinuities, only modes that share the same symmetry as the incident mode are created by mode conversion, whereas mode conversion to modes of different symmetry can occur with non-symmetric discontinuities. Experimental and numerical data show good agreement, revealing that the higher the order of the incident mode, the more complex the behaviour of the reflection coefficient is, as a function of the discontinuity depth. For the same incident mode, symmetric discontinuities impose less complexity than non-symmetric ones.**

***Keywords*—SH guided waves; mode conversion; PPM EMAT; wall thinning; reflection and transmission coefficients; symmetric discontinuities.**

1. Introduction

Ultrasonic guided waves are used widely for detecting defects, such as cracks and corrosion, in plates or pipes [1-4]. Non-destructive defect characterisation by means of ultrasonic guided waves relies on detecting the forward-scattered or back-scattered field produced by a guided wave mode that impinges on a defect [5]. Since the scattered field depends on the defect shape and size [6-8], comprehensive knowledge of the interaction of guided wave modes with defects is of great interest. Shear Horizontal (SH) waves are a family of guided waves that present in-plane particle motion, perpendicular to the direction of propagation. SH waves present some advantages, such as no energy leakage to surrounding non-viscous fluids, and they also have relatively simple dispersion relations compared to other guided wave modes. SH waves can be generated efficiently and detected in metallic samples with electromagnetic acoustic transducers (EMAT) [9-11].

Several authors investigated the interaction of SH guided wave in plates and torsional waves in pipes with notch and thickness discontinuities, that are commonly used to crudely describe corrosion-like defects [12-17]. Quantitative analysis is usually performed by calculating the reflection and transmission coefficient of the scattered waves [6, 12-14, 16-21]. Depending on the product of frequency and plate thickness, several SH modes can propagate, which can make interpretation of SH waves complicated. As a result, experiments are often restricted to the so-called low frequency-thickness regime, where only the SH0 mode or the T(0,1) mode, can propagate, in plates or pipes, respectively [6, 8, 12-14, 16, 18, 21-25]. Demma et al. investigated the scattering of the SH0 mode from rectangular notches in plates [12], and of the torsional mode T(0,1) in pipes [13], where both reflection from the notch leading edge and transmission away from the defect were analysed. The reflection and transmission from step-up and step-down thickness changes at low frequency were well approximated by simply considering an analogy of the thickness reduction with an acoustic impedance change. Wang et al. [24] numerically calculated the reflection and transmission coefficients for the circumferentially propagating SH0 mode with slots in pipes, that were used to simulate finite length axial cracks. More realistic defect geometries were also investigated, such as three-dimensional elliptical defects [22], tapered edge defects [6] and irregular shapes [8, 23, 26] and also overlap joint of plates [25].

In the high frequency-thickness regime, the interaction of guided waves with defects is more complicated, since the scattered waves may be composed of several propagating SH modes due to mode conversion [7, 15, 17, 19, 20]. Nurmalia et al. [7, 15] experimentally analysed the SH0 and SH1 modes in plates and the T(0,1) and T(0,2) modes in pipes [27] with gradual thickness reduction sections, showing that the interaction with defects depends on the thickness reduction rate. Recently, Kubrusly et al. [20] calculated the coefficients for reflection and transmission, for a large range of wall thinning depths and edge angles in plates, in a frequency-thickness product region where both the SH0 and SH1 were able to propagate. Kubrusly experimentally proved that mode conversion behaviour is complex, resulting in non-monotonic reflection and transmission coefficients. In the low frequency-thickness regime, the reflection and transmission coefficients tend to behave monotonically as a function of the discontinuity depth [12, 14, 16, 24].

Most published work considers discontinuities located on one of the surfaces of the plate, rather than being symmetrically present on both surfaces. Nevertheless, the interaction with symmetric discontinuities has also attracted the attention of researchers. Pau et al. analysed the reflection and transmission [16, 17] coefficients for the incident SH0 mode in both the low and high frequency-thickness regime in a plate with symmetric and non-symmetric notches. An analytical model was used in order to evaluate the coefficients as a function of the discontinuity depth and was further compared with finite element simulations. In the low-frequency thickness regime, no significant difference between the symmetric and non-symmetric discontinuities was observed [16, 17], whereas in the high-frequency regime [17] symmetric and non-symmetric discontinuities behave differently. It was observed that conversion to any propagating mode is allowed for non-symmetric discontinuities, whereas only symmetric modes were produced when a symmetric mode interacts with a symmetric discontinuity. Pau and Achillopoulou [19] extended their analysis for different geometries of the thinner section. Guided wave interactions with rectangular and elliptic profile notches and voids in the middle of the plate's cross-section were numerically simulated. Symmetric notches and voids allowed conversion to symmetric modes only, whereas non-symmetric notches and voids permitted mode conversion to modes of either symmetry. In both cases, the coefficients depend on the notch or void depth. Interestingly, for both low and high frequency-thickness cases, symmetric notches and voids in the middle of the plate present the same coefficient's values, and the elliptical and the rectangular notches showed similar results. Yan and Yuan [28] numerically analysed the conversion from the evanescent SH1 mode from either symmetric or non-symmetric apertures, such as a thinner section of a plate, into propagating modes in the full thickness section. In the former, the evanescent SH1 mode was converted only to the propagating SH1 mode, whereas in the latter, it was converted to either the propagating SH0 or SH1 modes.

The aforementioned papers show that the characteristics of the scattered waves depend on whether a discontinuity is symmetric or not; a symmetric mode can only be mode converted to symmetric modes when interacting with a symmetric discontinuity. However, no experimental validation was performed and only the propagating symmetric SH0 mode was used as the incident mode; the interaction of higher-order SH modes with symmetric or non-symmetric discontinuities was not investigated. It is indeed non-trivial to experimentally quantitative evaluate such phenomena, due to mode mixing of the several possible propagating modes, which render interpretation of the received signal complicated. In this paper, we address the interaction of the first four SH guided waves modes with thickness reduction discontinuities in plates in two different shapes, namely non-symmetric and symmetric, in order to analyse the mode conversion phenomena of symmetric and antisymmetric modes in these cases. Both experiments and numerical simulation were performed. Quantitative experimental data was obtained using the dual excitation and reception technique [29], which enables the calculation of the reflection and transmission coefficients for the discontinuity, considering all mode conversion possibilities.

2. SH guided waves

Shear horizontal guided waves have vibrational displacement perpendicular to the propagation direction and parallel to the plate's surface [30] which is given by:

$$u_z(x, y, t) = A_n U_n(y) e^{j(\omega t - \kappa_n x)}, \tag{1}$$

where x is the propagation direction, y is the coordinate of the plate thickness, z is the polarization direction, ω is the angular frequency, n is the mode order, κ_n, A_n and $U_n(y)$ are the wavenumber, amplitude and displacement profile of mode n, respectively. SH modes are usually classified as symmetric and antisymmetric according to their displacement profile, which can be described by:

$$U_n(y) = \cos(n\pi y/h + 3n\pi/2), \tag{2}$$

where h is the plate thickness. Symmetric modes have equal displacement at both surfaces ($y = \pm h/2$), whereas antisymmetric modes have displacement with the same absolute value, but of opposite sign at each surface. Even-order modes are symmetric, whereas odd-order modes are antisymmetric. Fig. 1(a) shows the displacement profile for modes SH0 to SH3. Apart from the fundamental zero-order SH0 mode, all other higher-order modes are dispersive and are only able to propagate for a frequency-thickness product above a cut-off value. At a fixed frequency, higher-order modes cannot propagate if the plate's thickness is below the cut-off thickness given by:

$$h_{\text{cut-off}} = n\, c_T/2f \;, \tag{3}$$

where c_T is the transverse wave speed and f is the frequency. For dispersive modes, the phase and group velocities depend on the frequency. Fig. 1(b) show the dispersion curves of SH guided wave modes for an 8 mm thick aluminium plate.

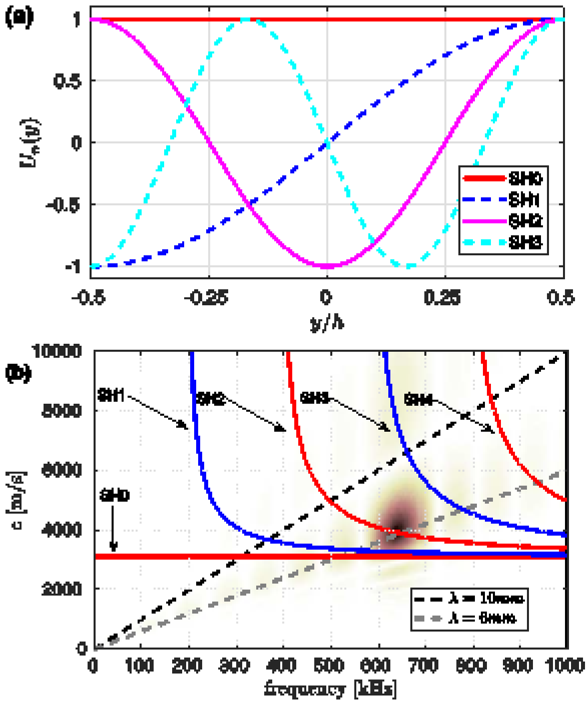

Fig. 1. (a) SH modes displacement profile. Continuous and dashed lines represent symmetric and antisymmetric modes, respectively. (b) Phase velocity dispersion curves of an 8 mm thick aluminium plate, red lines represent symmetric modes and blue lines, antisymmetric modes. The dashed lines represent a constant wavelength of 10 mm and 6 mm. The operating region for generation of the SH2 mode, centred at frequency 649 kHz and at 6 mm wavelength is shown behind the dispersion curves.

An ultrasonic wave carries energy whose power density is given by the vector [31]:

$$\boldsymbol{s} = -\frac{1}{2}\boldsymbol{v}^{*} \cdot \boldsymbol{\sigma} \;, \tag{4}$$

where $\boldsymbol{v}$ is the particle velocity vector, $\boldsymbol{\sigma}$ is the stress tensor and the asterisk means complex conjugate. For an SH guided wave mode, the relevant components of $\boldsymbol{v}$ and $\boldsymbol{\sigma}$ can be obtained from Eq. (1), yielding, respectively:

$$v_z = j\omega A_n U_n(y) e^{j(\omega t - \kappa_n x)} \ , \tag{5}$$

$$\sigma_{xz} = -j\mu\kappa_n A_n U_n(y) e^{j(\omega t - \kappa_n x)} \ . \tag{6}$$

where μ is the second Lamé constant. Therefore, the power density along the propagating direction for mode *n* is:

$$S_n = \frac{1}{2}\mu\omega\kappa_n U_n^2(y)|A_n|^2 \ , \tag{7}$$

and the power per unit width in the plate is given by the integral of S_n over the plate's height, which can be written as

$$P_n = E_n|A_n|^2 \ , \tag{8}$$

where E_n is here called the power level of the mode *n*, whose value is:

$$E_n = \frac{1}{2}\mu\omega\kappa_n \int_{y=-h/2}^{h/2} U_n^2(y)dy \ . \tag{9}$$

SH guided waves can be generated and detected with periodic permanent magnet (PPM) array EMATs, which consist of an array of magnets with an elongated spiral or "racetrack" coil underneath the PPM array [9, 10, 32]. The spacing or pitch of the magnets in the PPM EMATs imposes a nominal wavelength on the generated waves. Fig. 1(b) shows the nominal wavelength of a 10 mm and a 6 mm probe (straight dashed lines), superposed on the dispersion curves of the SH modes. The optimum excitation of a particular mode is achieved at the frequency where the wavelength line crosses the dispersion curve of this mode. Table I shows the optimum excitation frequency to generate SH modes, from order 0 to 3, used in this paper. However, due to the finite number of magnets in the array, the EMAT has a finite wavelength bandwidth of waves that can be excited [9]. Similarly, the excitation electric current applied to the coil produces a temporal bandwidth. The intersection of both bandwidths defines a region of operation, in which SH waves can be generated or received [3, 20, 29]. As an example, Fig. 1(b) shows the operating region for generating the SH2 mode, with a 3 cycle, 6 mm wavelength probe, using an 8 cycle tone burst at 649 kHz, which is the optimum frequency for SH2 generation. One can observe that the dispersion curve of the SH2 mode crosses the centre of this region.

Table I. Optimum excitation frequency for SH modes in an 8 mm thick aluminium plate and the possible mode conversions with their cut-off thicknesses; the value in parentheses means the maximum discontinuity relative depth (d/h) for a transmitted mode to propagate.

Nominal λ (mm)	Generated mode	Opt. excitation freq. (kHz)	Cut-off thicknesses of the possible mode conversions			
			SH0	SH1	SH2	SH3
10	SH0	311	0 mm	5.00 mm (37.5 %)	10.0 mm (–)	15.0 mm (–)
	SH1	367	0 mm	4.24 mm (47.0 %)	8.48 mm (–)	12.7 mm (–)
	SH2	498	0 mm	3.12 mm (61.0 %)	6.25 mm (21.9 %)	9.37 mm (–)
	SH3	662	0 mm	2.35 mm (70.6 %)	4.70 mm (41.3 %)	7.05 mm (11.9 %)
6	SH1	554	0 mm	2.81 mm (64.9 %)	5.62 mm (29.8 %)	8.43mm (–)
	SH2	649	0 mm	2.40 mm (70.0 %)	4.80 mm (40.1 %)	7.19 mm (10.12 %)
	SH3	782	0 mm	1.99 mm (75.1 %)	3.99 mm (50.3 %)	5.97 mm (25.4 %)

When a guided wave mode impinges upon some feature in the plate, such as a section with reduced thickness, the scattered field may be composed of several modes, i.e. the incident mode may suffer mode conversion either as reflection from the discontinuity or transmission to the thinner section [7, 15, 17, 19, 20]. Mode conversion to a propagating mode can arise only if its cut-off thickness, given by Eq. (3), is less than the plate's thickness. Table I also shows the possible converted modes, and their cut-off thickness, for incident modes from zero to third order, in an 8 mm thick aluminium plate. Cells marked with a dash mean that the mode conversion is not possible, due to the high cut-off thickness of the converted mode. It is worth highlighting that mode conversion with transmission to a thinner section of the plate can only happen if its remaining thickness is higher than the respective cut-off thickness; the percentage values in parentheses in Table I, give the maximum depth to original thickness value that a thinner section may have for a transmitted mode propagate.

3. Numerical and experimental investigation

3.1. Experimental setup and geometry

In order to analyse the interaction of SH waves, aluminium plates were machined with two types of discontinuity, namely symmetric and non-symmetric. In this case, a non-symmetric sample presents a discontinuity at a single surface with depth d, whereas a symmetric one presents discontinuity at both surfaces of the plate at the same longitudinal position, with each of their depths equal to $d/2$. Thus the total thickness reduction equals d in both cases. The test samples were 8 mm thick, 800 mm long and 250 mm wide aluminium plates. The geometry of the samples is shown in Fig. 2: the plate's plane lies in the x-z plane (thickness in the y-direction, length in the x-direction), the origin is defined as the position where the generating transducer is placed. The discontinuity is 150 mm long, ending 10 mm away from the right end of the plate, as shown in Fig. 2. The short section at the rightmost end of the plate plays no role in this study; this section had to remain with the original thickness in order to clamp the plates for machining. Here, only reflection and transmission at the leading edge of the discontinuity were investigated, transmission or reflection at the far end of the section was not analysed. The section at the left of the discontinuity was set to be long enough (640mm) in order to allow flexibility for the positioning of transducers. For each type of sample, three different total depths were machined, 2 mm, 4 mm and 6 mm, corresponding to 25 %, 50 % and 75 % of the original thickness, respectively.

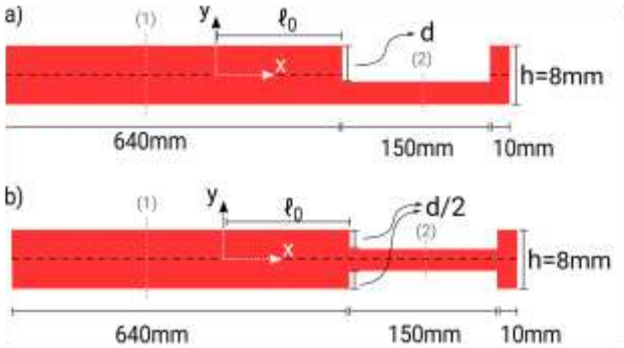

Fig. 2. Plate and discontinuity geometry. (a) Non-symmetric discontinuity. (b) Symmetric discontinuity.

Experiments were performed using a RITEC ® RPR-4000 Pulser/Receiver to generate and receive the signals from PPM EMATs, that were used as generator and receiver. The received signal was acquired by an oscilloscope that was connected to a PC to automate data acquisition. PPM EMATs were supplied by Sonemat Ltd, with either 10 mm or 6 mm nominal wavelength, all with a PPM array of 3 cycles (3 pairs of north-south orientated magnets along the length of the EMAT coil). Fig. 3 shows the experimental setup.

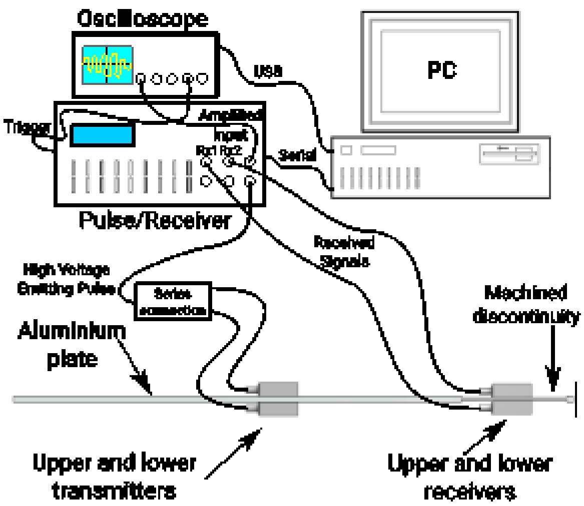

Fig. 3. Experimental setup

The excitation pulse was set to an 8 cycle tone burst at the optimum frequency for each mode, according to Table I. However, even at the optimum frequency, more than one mode can be generated or received if the dispersion curves of more than one mode intersect the operation region. For instance, in order to generate the SH2 with a 6 mm wavelength EMAT, one has to consider the operating region shown in Fig. 1(b). In this case, not only the intended mode is generated, but also the SH0 and SH1 modes are generated. Mode selection can be refined by adopting dual excitation on both surfaces of the plate [29]. This technique allows generation and reception of only symmetric or antisymmetric modes. Therefore, in the aforementioned example, apart from the SH2 mode, only the SH0 mode would be generated. Further differentiation of modes with the same symmetry was achieved by choosing an optimal receiving position, according to the modes' group velocity, to ensure that unwanted generated modes, or signals from mode conversion with the same symmetry, do not overlap in time. Considering the aforementioned example, since the group velocity of the SH0 and SH2 modes are considerably different, by carefully choosing the distance between the generation position and the discontinuity, distance ℓ_0 in Fig. 2, and the receiver position, either the unwanted generated SH0 mode or scattered waves from this mode can be separated in time. Similarly, by properly choosing the receiving position, one can detect the several modes that can arise due to mode conversion of the intended, SH2, mode without overlapping wave arrivals in time. The same principle applies for generation of the other modes. In this paper, ℓ_0 was set to a distance of between 73 mm to 110 mm, depending on the generated mode. The position of the receiver for direct and reflected waves was set at the left of the transmitter, position (1) in Fig. 2, either at -144 mm or -257 mm. Note that the direct wave could be received at a negative position because the EMAT generates SH waves that travel both forwards and backwards. In order to receive the transmitted waves, the receiver was positioned on the middle of the machined discontinuity, position (2) in Fig. 2. It is worth highlighting that modes with opposite symmetry can arrive at the same time at the receivers, since dual reception method ensures that symmetric and antisymmetric modes can be distinguished. Dual transduction has less restrictive experimental constraints than if a single transducer was used; for instance, shorter plates could be used. Even with dual transduction, generation of the SH0 mode at a 6 mm wavelength would result in excessively complicated interference, with generated and scattered waves needing to be resolved experimentally. At the optimum excitation frequency for the SH0 mode at 6 mm wavelength, the SH2 mode was also generated but with lower group velocity, therefore mixing in time with the scattered waves of interest, without providing a clear receiving position along the plate's length. Thus, the fundamental, SH0 mode was generated only with a nominal 10 mm wavelength probe, in order to ensure single mode generation, as shown in Table I; the remaining modes were generated at both 6 mm and 10 mm wavelengths.

3.2. Finite element model

Numerical analysis was performed using a commercial time-domain Finite Element Method (FEM) solver, PZFlex©, which allows simulation of SH waves in a two-dimensional model. Mirroring the experimental measurements, the symmetric and non-symmetric geometry of Fig. 2 were modelled, with aluminium density and transverse wave speed equal to 2698 kg/m^3 and c_T =3111 m/s, respectively. In the simulation, the parameter d was varied from 0 to 7.5 mm in 0.5 mm steps, in order to analyse the SH interaction as a function of the discontinuity depth more carefully. In order to generate the SH waves, a 3 cycle spatial force distribution function with a period of 10 mm or 6 mm was applied to the surface nodes of the model using a time history that was the same as the excitation current used in the experiment. This approach allows generation of SH guided waves, without the need of including the EMAT in the model, as validated previously elsewhere [3, 10, 29, 32]. Received signals were convolved with a 3 cycle spatial tone burst to simulate the receiving transducer spatial profile. As in the experiments, dual transmission at both surfaces of the plate was adopted to generate the SH guided wave modes.

Mode reception could be modelled likewise, replicating the setup used in the experiments. However, since numerical simulation allows one to access the displacement field for every point in the plate's cross-section, that is, as a function of y, each mode was effectively separated from the received signal based on the mode's orthogonality relationship [33-35]. The displacement profile, given by Eq. (2), forms an orthogonal basis, i.e,

$$\int_{y=-h/2}^{h/2} U_n(y)U_m(y)dy = \begin{cases} 0\ , & n \neq m \\ C_n\ , & n = m \end{cases}, \tag{10}$$

where

$$C_n = \int_{y=-h/2}^{h/2} U_n(y)U_n(y)dy = \begin{cases} h\ , & n = 0 \\ h/2, & n \neq 0 \end{cases}. \tag{11}$$

As the displacement field in the plate is composed of several SH modes, it can be expressed as:

$$u(x,y,t) = \sum_{m=0}^{N} A_m U_m(y) e^{j(\omega t - \kappa_m x)}, \tag{12}$$

where $u(x,y,t)$ is the displacement field as a function of x and y coordinates and time, t, and N is the number of SH modes. Therefore, thanks to the orthogonality relationship of Eq. (10), one can separate each mode present in the received signal through:

$$u_n(x,t) = \frac{1}{C_n} \int_{y=-h/2}^{h/2} u(x,y,t) U_n(y) dy, \tag{13}$$

such that $u_n(x,t)$ is the displacement field of mode n as a function of the longitudinal coordinate x and time. Normalization by the constant C_n is necessary to provide the proper dimensions and compensate for the weight of the displacement profile integral.

When compared to Lamb waves, the mode profile of SH guided waves is much simpler, involving a displacement or velocity component only in one direction, meaning that mode separation based upon the modes' orthogonality can be performed by means of a single field. Similar processing with Lamb waves [33, 34] requires one to acquire both displacement (or velocity) and stress in order to use the general orthogonality relationship [28]. In fact, in this case, the general orthogonality relationship yields Eq. (10), since for SH waves, the relevant non-zero particle velocity and stress components are scaled versions of the displacement profile, $U_m(y)$, as seen in Eq.(5) and (6).

The accuracy of the numerical computations and mode separation technique was assessed by calculating the energy balance of the scattered modes. The power of the incident and scattered modes was computed following Eq. (4): by multiplying the amplitude of the simulated velocity, v_z, and stress, σ_{xz}, fields of the reflected and transmitted modes as well as the incident mode, which were separated using the aforementioned post-processing. For the conservation of energy, the sum of the power of the scattered modes has to be equal to the incident mode's power. Or, equivalently,

$$1 = \sum_{j=1}^{N} \frac{P_{ij}^{-}}{P_i^{+}} + \sum_{j=1}^{N} \frac{P_{ij}^{+}}{P_i^{+}} , \tag{14}$$

where P_{ij}^{-} and P_{ij}^{+} are the power of the reflected and transmitted modes, respectively, of order j due to the incident mode i, whose power is P_i^{+}.The right-hand side of Eq. (14) was calculated for each incident mode at the simulated discontinuities depths and shapes analysed in this paper. Results were close to unity, confirming the accuracy of the numerical computations; the maximum error for each incident mode and discontinuity shape is shown in Table II.

Table 2 Maximum energy balance error in simulations.

Nominal λ (mm)	Generated mode	Maximum energy balance error (%)	
		Non-Symmetric discontinuity	Symmetric discontinuity

10	SH0	0.70	0.07
	SH1	3.08	1.77
	SH2	2.45	2.59
	SH3	2.69	2.69
6	SH1	1.08	2.47
	SH2	2.11	2.43
	SH3	6.05	4.51

3.3. Reflection and transmission coefficients

The coefficients for reflection from the discontinuity edge, R_{ij}, and transmission to the discontinuity, T_{ij}, are calculated, in order to perform quantitative analysis of the interaction of SH guided waves modes with either symmetric or non-symmetric discontinuities. The subscripts *i* and *j* in the coefficient notation represents the incident and received mode orders respectively. These coefficients are formally defined by:

$$R_{ij} = \frac{A_j^{(1)-}}{A_i^{(1)+}}, \qquad (15)$$

$$T_{ij} = \frac{A_j^{(2)+}}{A_i^{(1)+}} \sqrt{\frac{h-d}{h}}\ , \qquad (16)$$

where A is the maximum peak-to-peak amplitude of the received signal, the superscripts “+” and “-” mean the forward and backward propagating waves, respectively. The superscripts (1) and (2) indicate the reading positions: before the thinner region edge and on the thinner region, respectively, as shown in Fig. 2. Here, *i* and *j* can be 0 to 3, corresponding to the SH0 to SH3 modes, respectively. The square root in Eq. (16) is included to compensate for the natural amplitude increase of a wave when it is transmitted into a thinner region of the plate.

In order to calculate the coefficients, a time gate in which the forward or backward waves are expected to arrive was defined for each mode according to the receiving position, tone burst time duration and group velocity of the modes. When the thinner region remaining thickness is below the mode cut-off thickness, its group velocity is not a real number and thus a time gate for T_{i1}, T_{i2} or T_{i3} cannot be defined. Experimental and numerical signals were treated differently in this case. Experimental transmission coefficients were not calculated, because without a well-defined time gate, one cannot properly select the pulse relative to each mode. No time gate restriction was applied to calculate numerical coefficients since the several modes can be effectively separated through Eq. (13). This was done in order to allow analysis of any residual component inside the thinner section, when the cut-off thickness is exceeded. The same approach was applied to reflection coefficients of modes that cannot propagate in the original thickness section, dash marks in Table I.

In the interest of having meaningful values of the coefficients, compensation for amplitude reduction due to attenuation and mode dispersion was necessary. Compensation was performed by calculating the amplitude decay rate per propagated length in a non-machined plate for each generated mode, which was then used to compensate the amplitude of the received signals, considering the propagated distance at the receiving point. The propagated distance includes the forward and backward path, in the case of the reflection coefficient. When considering mode conversion, the compensation considered the proper mode in each part of the propagation path. For instance, when calculating the coefficient R_{21}, compensation should consider the mode SH2 along the forward path and the mode SH1 along the backward path. The only mechanism for amplitude decrease in the numerical simulation is pulse spreading due to dispersion since no damping was introduced in the simulation. Therefore, different compensating factors were used for experimental and numerical data. Nevertheless, once compensated, the coefficients could be straightforwardly compared.

4. Results

Fig. 4 (a) and (b) show a snapshot of the simulated particle velocity field due to the generation of the symmetric SH2 mode at 6 mm wavelength, in an 8 mm thick aluminium plate with 4 mm deep non-symmetric and symmetric discontinuities, respectively. The SH2 mode is generated at the origin and propagates to the left and the right. The wave propagating to the left is seen around -160 mm, which clearly shows the SH2 symmetric structure across the plate thickness. The wave propagating to the right interacts with the discontinuity, being mode converted to several modes, either as reflection or transmission into the discontinuity, which are indicated in Fig. 4. The wave structures of the SH3 and SH2 modes are clearly seen among the reflected waves at the non-symmetric discontinuity in Fig. 4(a). Moreover, the SH0 and SH1 modes can also be seen, mixed and ahead of the other modes due to their higher group velocity. The SH0 and SH1 modes are transmitted to the thinner region, where higher order modes cannot propagate due to their cut-off thickness (see Table I). Examining Fig. 4(b), one clearly sees that the interaction with a symmetric discontinuity differs from the non-symmetric case; there is mode conversion, either as reflection or transmission, uniquely to symmetric modes. Fig. 5 shows the wave field for the generation of the SH1 mode at 6 mm wavelength. In this case, since the incident mode is antisymmetric, the interaction with a symmetric discontinuity [Fig. 5(b)] allows mode conversion to antisymmetric modes only, whereas when the discontinuity is non-symmetric [Fig. 5(a)] all types of SH modes can be mode converted.

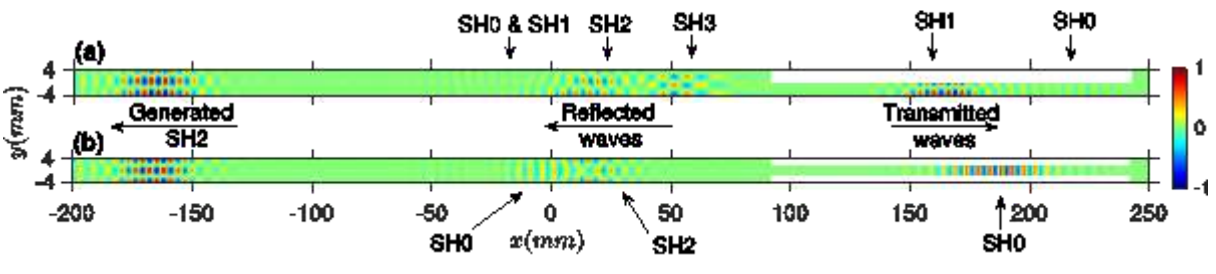

Fig. 4. Normalized particle velocity at 75 μs for a plate with 4 mm deep (a) non-symmetric and (b) symmetric discontinuity for generation of the SH2 mode at the origin.

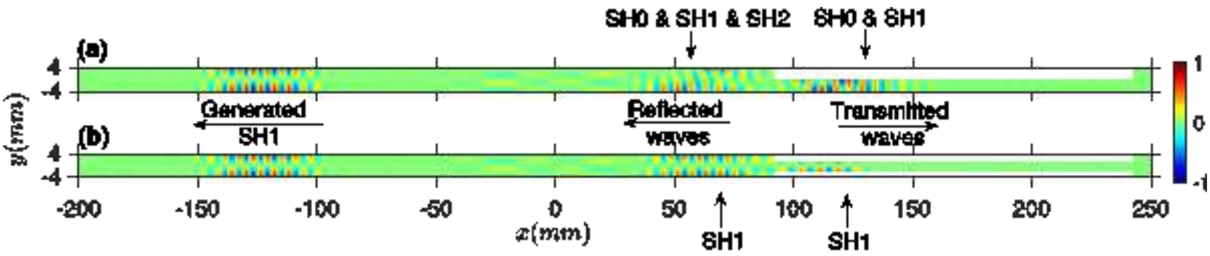

Fig. 5. Normalized particle velocity at 50 μs for a plate with 4 mm deep (a) non-symmetric and (b) symmetric discontinuity for generation of the SH1 mode at the origin.

Fig. 6 and Fig. 7 show the numerical and experimental received signals at -257 mm, with the origin set at $\ell_0 = 92$ mm, due to the generation of the SH2 mode at 6 mm wavelength interacting with 4 mm deep non-symmetric and symmetric discontinuities, respectively. The separated symmetric and antisymmetric parts of the experimental signals are shown in plots (a) and (b), respectively, whereas the numerical signals are shown in plots (c) and (d) in Fig. 6 and Fig. 7. The generated mode prior to interacting with the discontinuity is observable between 100 and 120 μs in plots (a) and (c), whereas the other wave packets correspond to the reflected waves from the discontinuity. Experimental signals have lower amplitude than simulated ones, as damping was not included in the simulation, and normalization was performed considering the direct wave that was not mode-converted. Considering the non-symmetric discontinuity (Fig. 6), the symmetric modes, SH2 and SH0, are received, around 180 μs and 150 μs, respectively, in Fig. 6(a). These modes can be separated in time due to the different group velocities, but the extent to which they can be clearly separated does depend on the receiving position: generally SH0 and SH2 may overlap in time, hindering identification. In fact, the reflected SH0 mode arrives between the direct SH2 signal and the reflected SH2 signal, as this receiving position was carefully chosen for this purpose. In this position one can also distinguish the antisymmetric modes, Fig. 6 (b) and (d). The SH1 mode arrives at around 160 μs and is clearly identified. The SH3 mode, on the other hand, is not clearly resolved in time; due to its low group velocity, it was expected to arrive at approximately 250 μs, being mixed with the reflected SH1 mode from the leftmost end of the plate, resulting in a complicated interfered signal. Therefore, this position is not ideal for clearly detecting this mode experimentally; indeed, a position closer to origin was chosen in order to properly calculate this mode amplitude without mode mixing. A cleaner mode separation is achieved within the numerically simulated signal by decomposition into the orthogonal basis, using Eq. (13). The separated signals are shown in Figs. 6 (c) and (d), where the individual modes are effectively separated even when they overlap.

The signals arising due to the interaction with a symmetric discontinuity are shown in Fig. 7, where one can see that the amplitude of the reflected SH0 modes is increased [Fig. 7 (a) and (b)], but mainly that signals associated with the antisymmetric modes have vanished [Fig. 7 (b) and (d)]. The low amplitude, experimental antisymmetric signal in Fig. 7(b) is due to the inherent imprecision of the experimental mode selectivity procedure, which is higher for selecting modes with opposite symmetry to the generated one [29], and is also possibly due to machining imprecision, which could result in a real discontinuity that is not perfectly symmetric. The highest difference between the depths of the machined discontinuities in both surfaces was measured at 0.13 mm which implies in about 6% of maximum symmetry error.

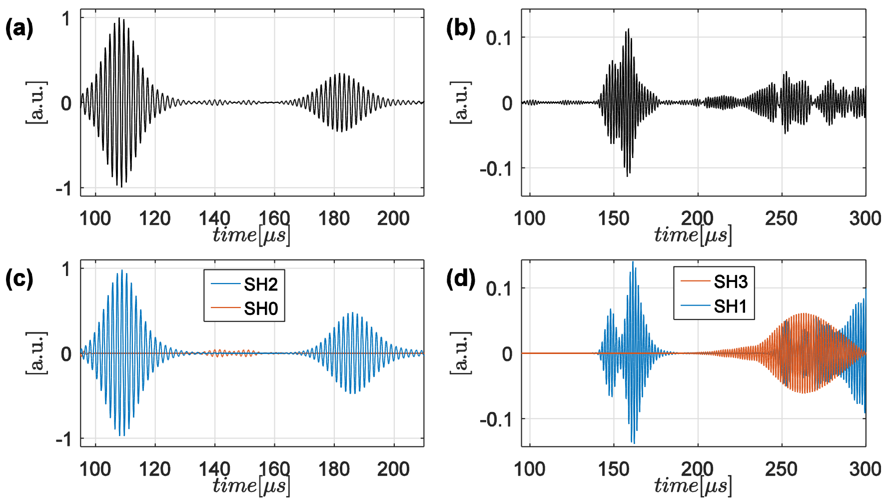

Fig. 6. Received signals at x = -257 mm due to the generation of SH2 at the origin interacting with a non-symmetric 4mm deep discontinuity starting at x=92mm. Experimental signals (a) and (b) and numerical signals (c) and (d). Symmetric modes (a) and (c) and antisymmetric modes (b) and (d).

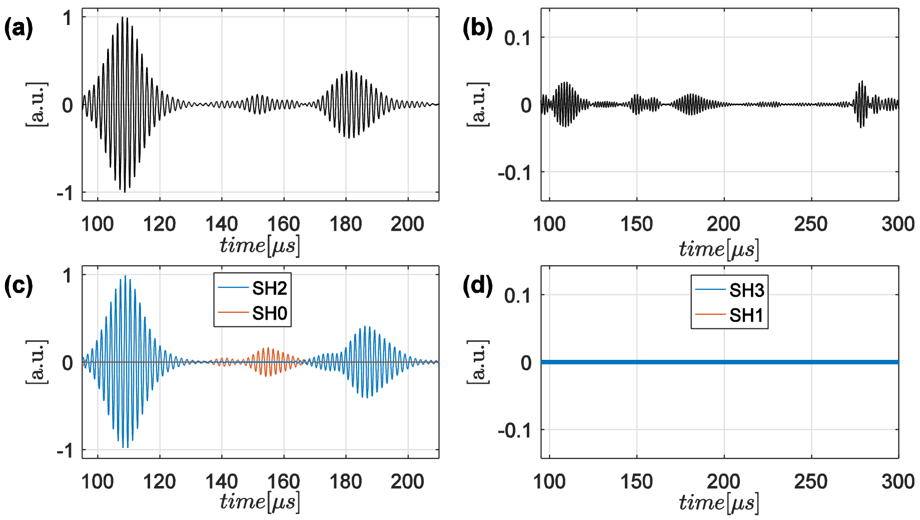

Fig. 7. Received signals at x = -257 mm due to the generation of SH2 at the origin interacting with a symmetric 4mm deep discontinuity starting at x=92mm. Experimental signals (a) and (b) and numerical signals (c) and (d). Symmetric modes (a) and (c) and antisymmetric modes (b) and (d).

The wave field in Fig. 4 and Fig. 5 and the experimental signals in Fig. 6 and Fig. 7 show that for a symmetric discontinuity, mode conversion occurs exclusively to modes with the same symmetry as the incident one, whereas all modes can be mode converted due to the interaction with a non-symmetric discontinuity. Theoretically, this happens because a symmetric discontinuity presents identical boundary conditions in both surfaces of the plate, therefore imposing that the scattered field in both halves of the plate behaves equally with respect to the plate's mid-plane, which consequently restricts mode-conversion within the same type of symmetry of the incident mode. On the other hand, in a non-symmetric discontinuity, there is no symmetry on the boundary conditions and therefore, any mode-conversion is allowed. Also, the intensity of the reflected and transmitted modes differs in both cases, depending on whether the discontinuity is symmetric or non-symmetric. In order to perform further analysis, quantitative data is obtained by calculating the reflection and transmission coefficients, according to Eqs. (15) and (16), respectively. The reflection coefficients due to non-symmetric and symmetric discontinuities as a function of the discontinuity depth are shown in Fig. 8 and Fig. 9, respectively. Experimental and numerical data for 10 mm and 6 mm nominal wavelengths are shown. Solid lines and circles represent signals obtained with a transducer of 10 mm wavelength, either numerically or experimentally, respectively. Dashed lines and crosses represent results for the 6 mm wavelength transducer, either numerically or experimentally, respectively.

Incident symmetric modes, either the SH0 or SH2 modes, are shown in plots (a) and (c), respectively. One can clearly see that for the symmetric discontinuity, Fig. 9(a) and (c), there is mode conversion uniquely to symmetric modes, whereas all modes can potentially be mode converted due to the interaction with a non-symmetric discontinuity, Fig. 8 (a) and (c). This experimentally confirms the numerical results of Pau et al. [17, 19], who analysed the incident SH0 mode. The coefficients for incident antisymmetric modes, either the SH1 or SH3, are shown in plots (b) and (d), respectively. In this case, a symmetric discontinuity leads only to antisymmetric modes arising from mode conversion. As shown in Table I, at the optimum excitation frequency and wavelength used to generate each of the SH modes, not all of the other modes can propagate due to their cut-off thickness. Accordingly, only conversions to the predicted allowed modes were experimentally and numerically detected in Fig. 8 and Fig. 9. The intensity of the converted modes is higher with a wavelength of 6 mm than a wavelength of 10 mm, because the dispersion curves of the shorter wavelength guided waves are closer to each other in the frequency-phase velocity plane. Therefore, converted modes are received with higher intensity due to the finite operating region [see Fig. 1(b)].

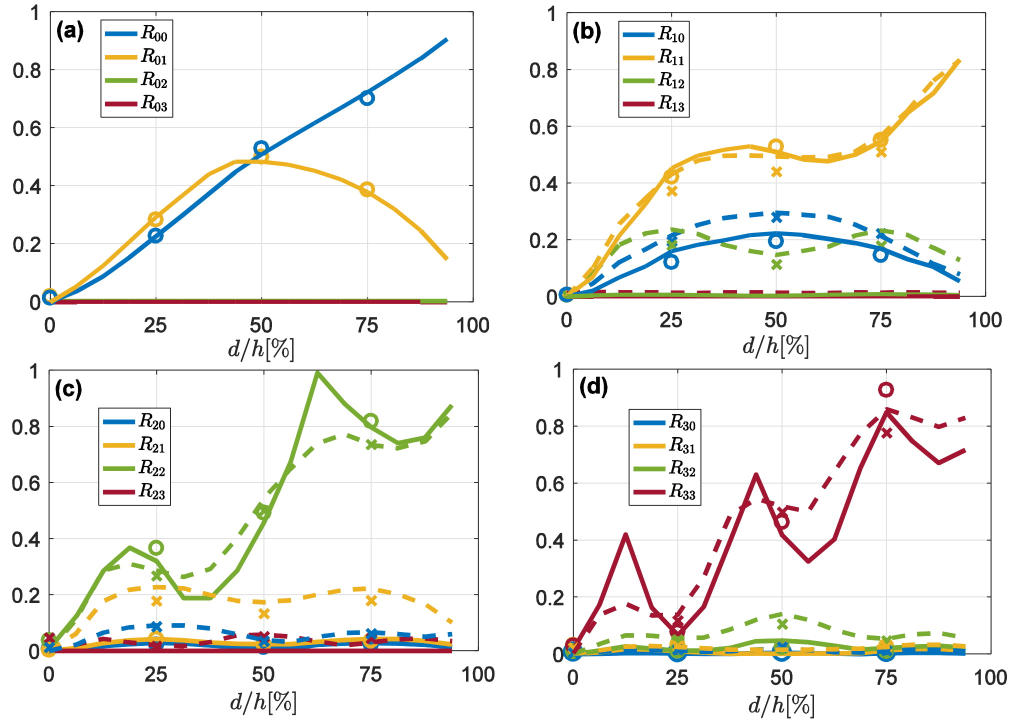

Fig. 8. Numerical (lines) and experimental (symbols) reflection coefficient versus discontinuity depth for a non-symmetric discontinuity due to incident (a) SH0, (b) SH1, (c) SH2 and (d) SH3. Solid lines and circles represent transducer wavelength of 10 mm and dashed lines and crosses represent 6 mm transducer wavelength.

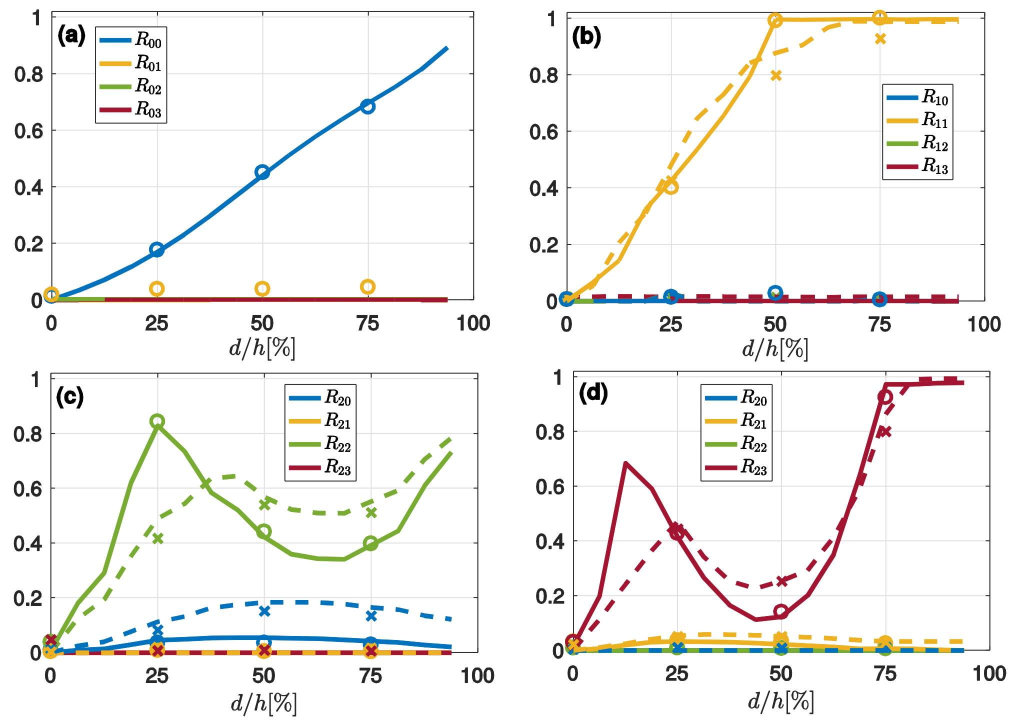

Fig. 9. Numerical (lines) and experimental (symbols) reflection coefficient versus discontinuity depth for a symmetric discontinuity due to incident (a) SH0, (b) SH1, (c) SH2 and (d) SH3. Solid lines and circles represent transducer wavelength of 10 mm and dashed lines and crosses represent 6 mm transducer wavelength.

The transmission coefficient due to non-symmetric and symmetric discontinuity is shown in Fig. 10 and Fig. 11, respectively. Due to the mode cut-off thickness, transmission coefficient to non-fundamental modes must eventually tend to zero as the discontinuity depth increases. This behaviour can be verified in Fig. 10 and Fig. 11, and the relative depths in which the coefficients approach zero correspond to the ones theoretically calculated in Table I, either for 10 mm or 6 mm wavelengths. The same mode conversion behaviour regarding the discontinuity symmetry is valid for the transmitted waves; i.e., within a symmetric discontinuity there can be mode conversion to modes that share the same symmetry condition as the incident modes, either symmetric or antisymmetric. Generally, numerical and experimental data show good agreement.

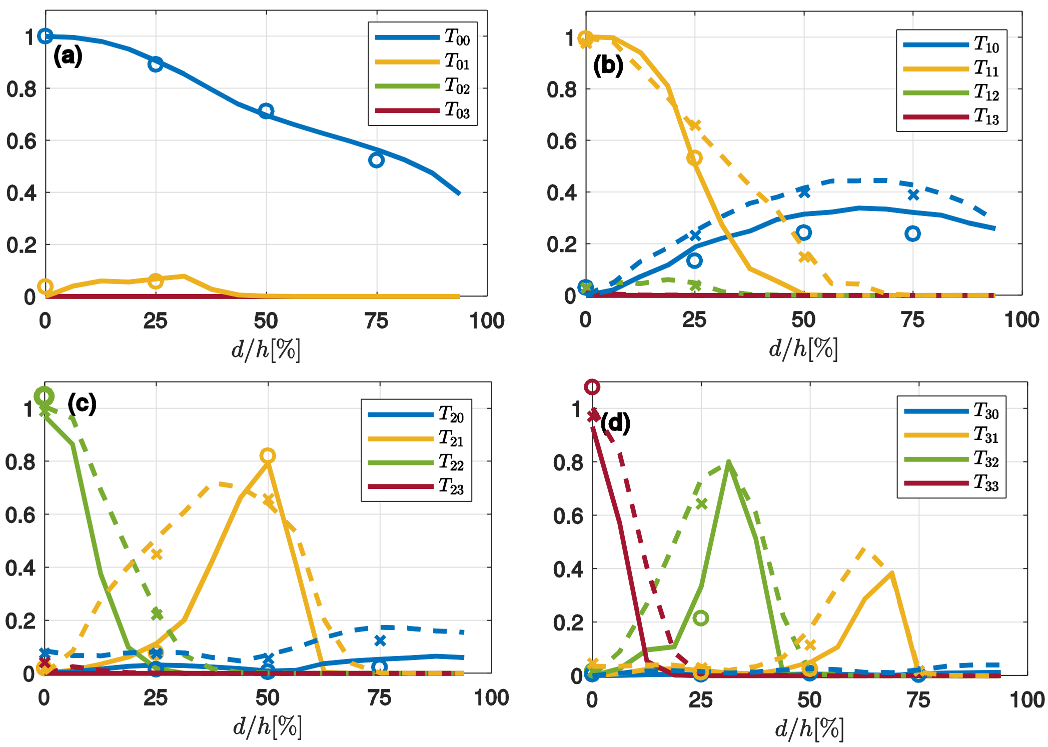

Fig. 10. Numerical (lines) and experimental (symbols) transmission coefficient versus discontinuity depth for a non-symmetric discontinuity due to incident (a) SH0, (b) SH1, (c) SH2 and (d) SH3. Solid lines and circles represent transducer wavelength of 10 mm and dashed lines and crosses represent 6 mm transducer wavelength.

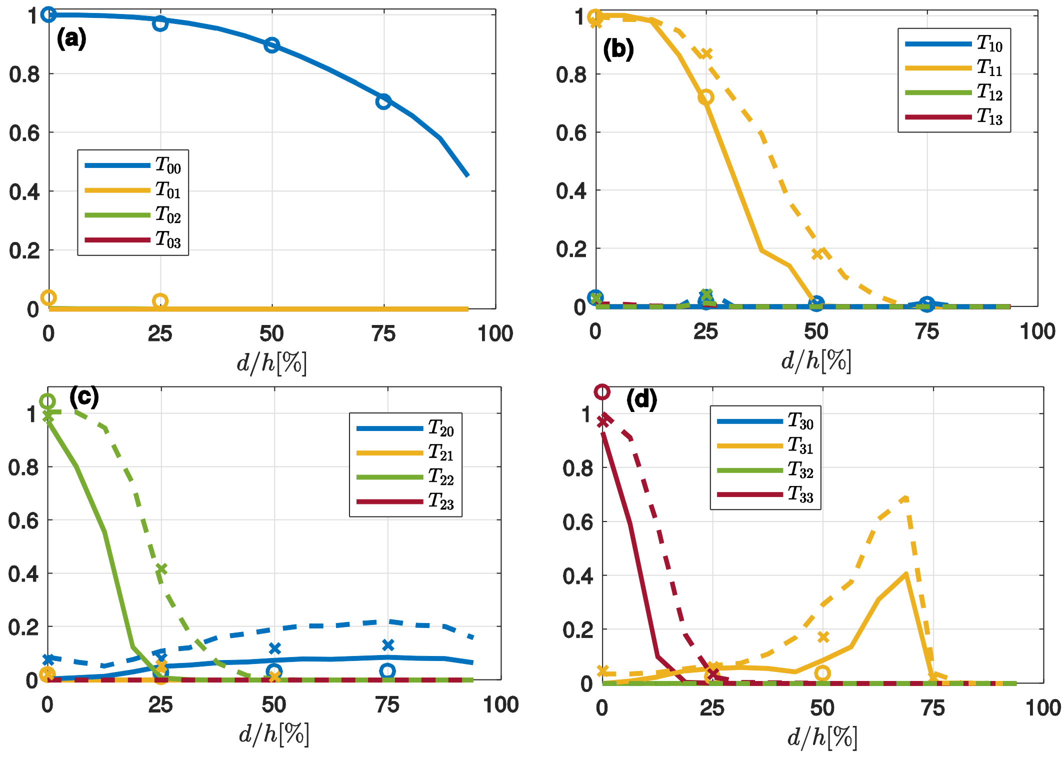

Fig. 11. Numerical (lines) and experimental (symbols) transmission coefficient versus discontinuity depth for a symmetric discontinuity due to incident (a) SH0, (b) SH1, (c) SH2 and (d) SH3. Solid lines and circles represent transducer wavelength of 10 mm and dashed lines and crosses represent 6 mm transducer wavelength.

5. Discussion

Previous work [20] has shown that the coefficients for incident SH0 and SH1 modes, in a frequency-thickness product value in which only these two modes can propagate, behave non-monotonically, unlike at the low frequency-thickness value, where coefficients are monotonic [16, 24]. Here, higher order modes were used as incident modes, and it is observed that the higher the order of the generated mode, the more intense the non-monotonic behaviour of the coefficients is. In Fig. 8, the R_{00} coefficient shows a linear behaviour whereas, R_{11} presents a zero derivative point for around half thickness discontinuity with 6 mm wavelength, and one local maximum point with 10 mm wavelength, and R_{22} and R_{33} show two and three local maxima points, respectively. The peaks in the reflection coefficient occur at discontinuity depths that correspond to the remaining thicknesses being slightly higher than the cut-off thicknesses of the SH modes. One should also note that for a larger generated wavelength, where the operating frequency is closer to the mode cut-off frequency-thickness and dispersion is at its highest [see Fig. 1(b)], the non-monotonicity is yet more acute, i.e. the peaks and troughs are more well defined, as it can be seen comparing the solid and dashed lines for R_{22} and R_{33} in Fig. 8 (c) and (d). Interestingly for symmetric discontinuities, the non-monotonic behaviour is less accentuated, typically with fewer oscillations (see Fig. 9).

The values for the reflection and transmission coefficients, observed in Figs. 8 to 11, are a consequence of the boundary condition at the discontinuity and the energy conservation principle. Some of the interesting behaviour as a function of the discontinuity depth can be explained from consideration of ultrasonic energy or power. The incident mode carries energy which is proportional to its power level, E_n, defined in Eq.(9). Note that E_n, does not include the amplitude of the mode, the power is given by Eq.(8), in which E_n is multiplied by the square of displacement amplitude. At a fixed frequency, a high-order mode has higher phase velocity, (see Fig. 1(b)), and consequently lower wavenumber and, therefore, a lower power level (see Eq.(9)) than the other possible propagating modes. Since the energy of the incident mode has to be redistributed among the scattered modes, one can expect that the amplitude of a scattered high-order mode should be higher than that of a lower-order mode, since the latter has a higher power level. Fig. 12(a) shows the power level of the reflected and transmitted SH modes normalized per the power level of the incident SH3 at 662 kHz, calculated from Eq.(9), considering the actual wavenumber value inside the discontinuity. Following this reasoning, the values of the reflection and transmission coefficients to higher-order modes are expected to be higher than those to lower-order modes. Taking, for instance, the SH3 as the incident mode, when the discontinuity is shallow, energy balance is almost completely satisfied by a high transmission coefficient to the same-order mode, i.e., the SH3 mode, as can be seen in Fig. 10(d). As the depth increases, this mode's cut-off thickness is approached to a point at which it can no longer propagate, i.e. it carries no energy. Simultaneously, the amplitude of the reflected SH3 mode increases until reaching a peak [Fig. 8(d)], when the thickness of the thinner section is equal to this mode cut-off thickness. When the discontinuity depth increases further, the power level of the SH2 mode inside the thinner section decreases, approaching the power level of the incident SH3 mode, (see Fig.12.(a) at about $20\% < d/h < 40\%$), because its wavenumber decreases in the thinner section - recall that its phase velocity increases for a lower thickness [11]. Thus the transmission of the SH2 mode is maximized [Fig. 10(d)] and the reflection of the SH3 mode decreases [Fig. 8(d)]. If discontinuity depth keeps increasing, the SH2 mode can no longer propagate inside the thinner section, and reflection of the SH3 mode again reaches a peak [Fig. 8(d)]. This also happens for the SH1 mode, in the discontinuity, Fig.12.(a) at about $40\% < d/h < 70\%$. This mechanism of preferred energy swapping between reflection to the same-order mode and transmission to the highest order mode that is able to propagate in the thinner section, therefore explains the occurrence of peaks in the reflection and transmission coefficients in the same quantity as the order of the incident mode, observed in Fig. 8.

For symmetric discontinuities, the same principle holds if skipping consecutive modes, since only modes that share the same symmetry as the incident mode can be created in this case. Therefore, it is expected that the peaks for the reflection of the same-order mode to be even higher. Following the example for the incident SH3 mode, when its transmission is no longer possible, because the thickness of the thinner region is less than its cut-off thickness, then the reflection of the SH3 mode should be even stronger. The antisymmetric mode with the closest power level is the SH1 mode, whose power level is elevated [see Fig.12(a)], and thus would have a lower amplitude. The higher values for the peaks within a symmetric discontinuity can be verified comparing Fig.9(d) and Fig.8(d).

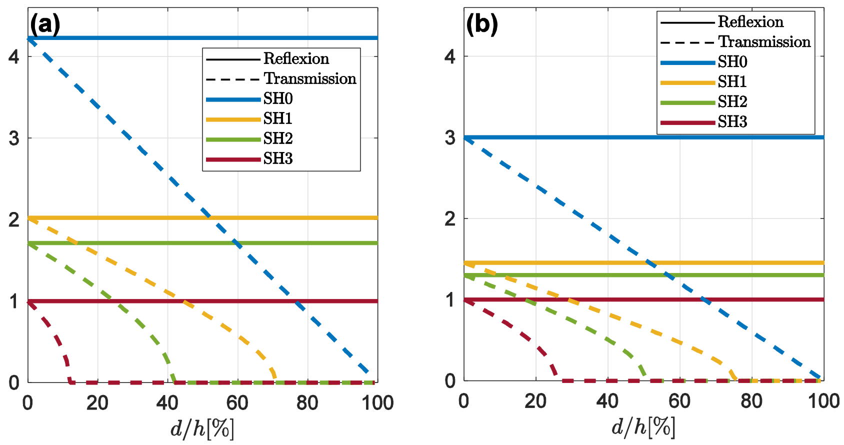

Figure 12 Power level for reflected (solid lines) and transmitted (dashed) modes normalized per the power level of the incident SH3 mode at (a) 662 kHz and (b) 782 kHz as a function of the discontinuity depth. The power level of a transmitted mode reaches zero at its respective cut-off thickness.

When a higher-order mode is generated at a lower wavelength, and consequently, higher wavenumber, its power level is closer to the other modes, see Fig. 12.(b), and therefore, the intensity of scattered modes is more equally distributed. Consequently, the difference between peaks and valleys in the reflection coefficient is less accentuated, since the aforementioned preferred energy swap mechanism is no longer valid, as more modes significantly participate in the energy redistribution.

The peaks in the reflection coefficient of higher-order modes could suggest interesting applications in NDT, if a higher amplitude reflection from a shallow discontinuity of a specific critical value is intended. For instance, a possible application would be to detect the presence of a defect of a specific depth or to monitoring the growth of a discontinuity. In this potential application, one would set the operating wavelength and frequency close to the cut-off frequency and the resulting cut-off thickness should match the remaining thickness that corresponds to a critical depth of interest. When the discontinuity depth approaches the critical value an intense reflection is received, facilitating detection.

6. Conclusion

The interaction of fundamental and higher-order SH guided wave modes with symmetric and non-symmetric thickness discontinuities in plates was experimentally and numerically analysed through quantitative data. Experimentally, generation and receiving positions had to be chosen carefully, to avoid mode mixing. Dual transduction helps to avoid mode mixing by separating symmetric and antisymmetric modes. Numerically, an orthogonal mode decomposition, post-processing method allowed effective mode separation.

It was experimentally confirmed that mode conversion depends not only on the thinning depth but also on its symmetry. All possible mode conversions can occur in non-symmetric discontinuities, whereas only mode conversion to modes with the same type of symmetry of the incident mode can happen due to the interaction with a symmetric discontinuity. The investigation of incident higher-order modes also revealed that the reflection coefficient of higher-order modes present even stronger non-monotonicity as a function of the discontinuity depth, which is reduced when the discontinuity is symmetric. Additionally, one can conclude that at a lower frequency, closer to the cut-off frequency of the incident mode, the behaviour of the reflection and transmission coefficients presents yet more accentuated variations over the discontinuity depth range. There are peaks in the reflection coefficient of the same mode as the incident one, and in the transmission coefficient to lower-order modes at discontinuity depths that correspond to remaining thicknesses close to the cut-off thicknesses. This behaviour is explained by consideration of the proposed mechanism based on the energy conservation principle.

This paper's results further elucidate the interaction of SH guided waves with a thickness discontinuity section. The different behaviour between symmetric and non-symmetric discontinuities was experimentally demonstrated, also showing that the behaviour of higher-order SH modes is yet more complex and highly dependent not only on the discontinuity depth but also on its positioning in the plate’s cross-section and on the frequency.

Acknowledgements

Authors would like to thank the Brazilian National Council for Scientific and Technological Development, CNPq, for financial support.

References

[1] M. Hirao and H. Ogi, "An SH-wave EMAT technique for gas pipeline inspection," *NDT & E International,* vol. 32, no. 3, pp. 127-132, 1999/04/01/ 1999

[2] S. Dixon, S. E. Burrows, B. Dutton, and Y. Fan, "Detection of cracks in metal sheets using pulsed laser generated ultrasound and EMAT detection," *Ultrasonics,* vol. 51, no. 1, pp. 7-16, 2011.

[3] M. Clough, M. Fleming, and S. Dixon, "Circumferential guided wave EMAT system for pipeline screening using shear horizontal ultrasound," vol. 86, pp. 20-27, 2017.

[4] Nurmalia, N. Nakamura, H. Ogi, and M. Hirao, "EMAT pipe inspection technique using higher mode torsional guided wave T(0,2)," *NDT & E International,* vol. 87, pp. 78-84, 2017/04/01/ 2017.

[5] Y. Shen and V. Giurgiutiu, "Combined analytical FEM approach for efficient simulation of Lamb wave damage detection," *Ultrasonics,* vol. 69, pp. 116-128, 2016/07/01/ 2016.

[6] R. Carandente, J. Ma, and P. Cawley, "The scattering of the fundamental torsional mode from axi-symmetric defects with varying depth profile in pipes," (in eng), *J Acoust Soc Am,* vol. 127, no. 6, pp. 3440-8, Jun 2010.

[7] Nurmalia, N. Nakamura, H. Ogi, M. Hirao, and K. Nakahata, "Mode conversion behavior of SH guided wave in a tapered plate," vol. 45, no. 1, pp. 156-161, 2012.

[8] R. Carandente and P. Cawley, "The effect of complex defect profiles on the reflection of the fundamental torsional mode in pipes," *NDT & E International,* vol. 46, pp. 41-47, 2012/03/01/ 2012.

[9] S. Dixon, P. A. Petcher, Y. Fan, D. Maisey, and P. Nickolds, "Ultrasonic metal sheet thickness measurement without prior wave speed calibration," *Journal of Physics D: Applied Physics,* vol. 46, no. 44, p. 445502, 2013.

[10] P. A. Petcher, S. E. Burrows, and S. Dixon, "Shear horizontal (SH) ultrasound wave propagation around smooth corners," vol. 54, no. 4, pp. 997-1004, 2014.

[11] W. Luo and J. L. Rose, "Guided wave thickness measurement with EMATs," *Insight - Non-Destructive Testing and Condition Monitoring,* vol. 45, no. 11, pp. 735-739, // 200.

[12] A. Demma, P. Cawley, and M. Lowe, "Scattering of the fundamental shear horizontal mode from steps and notches in plates," *The Journal of the Acoustical Society of America,* vol. 113, no. 4, pp. 1880-1891, 2003.

[13] A. Demma, P. Cawley, M. Lowe, and A. G. Roosenbrand, "The reflection of the fundamental torsional mode from cracks and notches in pipes," *The Journal of the Acoustical Society of America,* vol. 114, no. 2, pp. 611-625, 2003.

[14] A. Demma, P. Cawley, M. Lowe, A. G. Roosenbrand, and B. Pavlakovic, "The reflection of guided waves from notches in pipes: a guide for interpreting corrosion measurements," *NDT & E International,* vol. 37, no. 3, pp. 167-180, 2004/04/01/ 2004.

[15] H. Nurmalia and Nobutomo Nakamura and Hirotsugu Ogi and Masahiko, "Detection of Shear Horizontal Guided Waves Propagating in Aluminum Plate with Thinning Region," *Japanese Journal of Applied Physics,* vol. 50, no. 7S, p. 07HC17, 2011.

[16] D. Achillopoulou, A. Pau, and F. Vestroni, *Damage characterization in waveguides with ultrasonic shear waves*. 2015.

[17] A. Pau, D. V. Achillopoulou, and F. Vestroni, "Scattering of guided shear waves in plates with discontinuities," *NDT & E International,* vol. 84, pp. 67-75, 2016/12/01/ 2016.

[18] P. Rajagopal and M. J. S. Lowe, "Scattering of the fundamental shear horizontal guided wave by a part-thickness crack in an isotropic plate," *The Journal of the Acoustical Society of America,* vol. 124, no. 5, pp. 2895-2904, 2008.

[19] A. Pau and D. V. Achillopoulou, "Interaction of Shear and Rayleigh-Lamb Waves with Notches and Voids in Plate Waveguides," (in eng), *Materials (Basel),* vol. 10, no. 7, Jul 2017.

[20] A. C. Kubrusly, M. A. Freitas, J. P. von der Weid, and S. Dixon, "Interaction of SH guided waves with wall thinning," *NDT & E International,* vol. 101, pp. 94-103, 2019/01/01/ 2019

[21] J. Combaniere, P. Cawley, K. McAughey, and J. Giese, "Interaction Between SH_0 Guided Waves and Tilted Surface-Breaking Cracks in Plates," *IEEE Transactions on Ultrasonics, Ferroelectrics, and Frequency Control,* vol. 66, no. 1, pp. 119-128, 2019.

[22] J. Ma and P. Cawley, "Low-frequency pulse echo reflection of the fundamental shear horizontal mode from part-thickness elliptical defects in plates," (in eng), *J Acoust Soc Am,* vol. 127, no. 6, pp. 3485-93, Jun 2010.

[23] R. Carandente, A. Lovstad, and P. Cawley, "The influence of sharp edges in corrosion profiles on the reflection of guided waves," *NDT & E International,* vol. 52, pp. 57-68, 2012/11/01/ 2012.

[24] S. Wang, S. Huang, W. Zhao, and Z. Wei, "3D modeling of circumferential SH guided waves in pipeline for axial cracking detection in ILI tools," *Ultrasonics,* vol. 56, pp. 325-331, 2015/02/01/ 2015.

[25] Y. Ho Cho, J. L. Rose, and H. Geon Kwun, "SH Guided Wave Scattering in a Structure with Thickness Variation," vol. 321-323, pp. 792-794, 2006.

[26] L. Moreau, A. Velichko, and P. D. Wilcox, "Accurate finite element modelling of guided wave scattering from irregular defects," *NDT & E International,* vol. 45, no. 1, pp. 46-54, 2012/01/01/ 2012.

[27] H. Nurmalia and Nobutomo Nakamura and Hirotsugu Ogi and Masahiko, "Mode Conversion and Total Reflection of Torsional Waves for Pipe Inspection," *Japanese Journal of Applied Physics,* vol. 52, no. 7S, p. 07HC14, 2013.

[28] X. Yan and F.-G. Yuan, "A semi-analytical approach for SH guided wave mode conversion from evanescent into propagating," *Ultrasonics,* vol. 84, pp. 430-437, 2018/03/01/ 2018.

[29] A. Kubrusly, M. d. A. Freitas, J. P. von der Weid, and S. Dixon, "Mode selectivity of SH guided waves by dual excitation and reception applied to mode conversion analysis.," *Ultrasonics, Ferroelectrics and Frequency Control, IEEE Transactions on,* vol. to be published, 2018.

[30] J. L. Rose, *Ultrasonic Guided waves in solid media*. Cambridge University Press, 2014.

[31] B. A. Auld, *Acoustic fields and waves in solids,* 2nd ed. ed. Malabar, Fla.: R.E. Krieger, 1989.

[32] P. A. Petcher and S. Dixon, "Mode mixing in shear horizontal ultrasonic guided waves," *Nondestructive Testing and Evaluation,* pp. 1-20, 2016.

[33] G. Shkerdin and C. Glorieux, "Lamb mode conversion in a plate with a delamination," *The Journal of the Acoustical Society of America,* vol. 116, no. 4, pp. 2089-2100, 2004/10/01 2004.

[34] L. Moreau, M. Castaings, B. Hosten, and M. V. Predoi, "An orthogonality relation-based technique for post-processing finite element predictions of waves scattering in solid waveguides," *The Journal of the Acoustical Society of America,* vol. 120, no. 2, pp. 611-620, 2006/08/01 2006.

[35] X. Yan and F.-G. Yuan, "Conversion of evanescent Lamb waves into propagating waves via a narrow aperture edge," *The Journal of the Acoustical Society of America,* vol. 137, no. 6, pp. 3523-3533, 2015/06/01 2015.